Experimental Evaluation of a CPT-Based Four-Leg Active Power Compensator for Distributed Generation

Claudio Burgos-Mellado, Carlos Hernández-Carimán, Roberto Cárdenas, *Senior Member, IEEE*, Doris Sáez, *Senior Member, IEEE*, Mark Sumner, *Senior Member, IEEE*, Alessandro Costabeber, *Member, IEEE*, and Helmo K. Morales Paredes, *Member, IEEE*

***Abstract*— Four-wire microgrids (MGs) and distribution systems are inherently unbalanced with the presence of negative and zero sequence components in voltages and currents. In small autonomous systems, the imbalance, in addition to the harmonic distortion produced by nonlinear loads, can significantly affect the power quality, loadability, and stability of the system. Furthermore, in isolated networks with significant generation from intermittent renewable energy sources, the stiffness of the system is reduced and this could amplify the effects of imbalance on the stability and power quality. To mitigate some of these problems, a novel methodology based on the application of a four-leg active power filter is proposed in this paper. The control of the compensator is based on the conservative power theory augmented by resonant controllers. The behavior of the proposed system is demonstrated using an experimental prototype deployed in a laboratory scale MG.**

***Index Terms*— Active power filter (APF), conservative power theory (CPT), harmonic distortion, imbalance, microgrids (MGs), resonant control.**

I. Introduction

POWER systems are undergoing a paradigm change, moving from centralized distribution to distributed generation including microgrids (MGs) and smart grids. In distributed generation systems, it is expected that a relatively high penetration of electrical energy provided by nonconventional renewable energy (NCRE) sources of intermittent nature will be present, usually connected to the MG using power electronic converters that can affect the stiffness of the network. Droop control is one of the methods typically used to share active and reactive power between these generating units [1], [2], and this may lead to some variations in the MG fundamental frequency: this must be considered when designing control systems for active power filter (APF) applications.

An MG could be implemented as a low-voltage power distribution system operating in grid connected or islanded mode [3]–[5] feeding single-phase linear and nonlinear loads, typically using three-phase four-wire topologies [6], [7]. These inherently unbalanced loads produce negative and zero sequence components in the currents and voltages of the network. According to [8], the ratio of unbalanced to balanced loads will increase in the future with higher penetration of hybrid and electric vehicles, heat pumps, and so on. In this context, some well-known problems related to load imbalance could appear [9]. For instance, negative sequence voltage components produce oscillations in the torque of induction machines and synchronous generators. This in turn may reduce the efficiency and useful life of these machines [8], [10]. Other effects of imbalance are localized heating in machines and power converters, and reduced loadability of conventional synchronous generators (see [10], [11]), which affects the stability of the MGs [11]. The zero sequence current flowing through the neutral wire can produce additional problems such as overloading of the neutral conductor [9], [12] and malfunction of sensitive equipment due to ground voltage fluctuations if the current flowing through the neutral wire is large and/or the impedance of the neutral connection has a relatively large magnitude [9], [12]. In addition, the load served by a four-leg MG could be of nonlinear nature [12]–[14], generating distorted load currents that could also diminish the loadability of the power generating sources in the MG.

Several solutions have been proposed in the literature to compensate for imbalance and harmonic distortion [15]–[17]. Among them, APFs are considered appropriate topologies with several papers discussing issues such as the design of the APF's passive components [6], [12], compensation objectives [8], [18], and serial and/or parallel connection of APFs [6]. The performance of the APF is heavily dependent on the control system applied, which is usually based on a power theory, with many applications using the p–q or modified p–q power theories. However, one of the reported disadvantages of these methodologies is their sensitivity to distortion in

Manuscript received June 30, 2016; revised October 3, 2016; accepted November 10, 2016. Date of publication November 24, 2016; date of current version May 1, 2017. This work was supported in part by Conicyt under Grant FONDECYT 1140775 and Grant FONDEF ID14I10063 and in part by Conicyt-Basal under Project FB0008. Recommended for publication by Associate Editor Xiongfei Wang.

C. Burgos-Mellado, C. Hernández-Carimán, R. Cárdenas, and D. Sáez are with the Department of Electrical Engineering, Facultad de Ciencias Físicas y Matemáticas, University of Chile, 8370451 Santiago, Chile (e-mail: rcardenas@ing.uchile.cl).

M. Sumner and A. Costabeber are with the PEMC Group, University of Nottingham, NG72RD, Nottingham, U.K. (e-mail: mark.sumner@nottingham.ac.uk).

Helmo K. Morales Paredes is with São Paulo State University (Unesp), Institute of Science and Technology, Sorocaba, 18087-180 Sorocaba, Brazil (e-mail: hmorales@sorocaba.unesp.br).

Color versions of one or more of the figures in this paper are available online at http://ieeexplore.ieee.org.

Digital Object Identifier 10.1109/JESTPE.2016.2633064

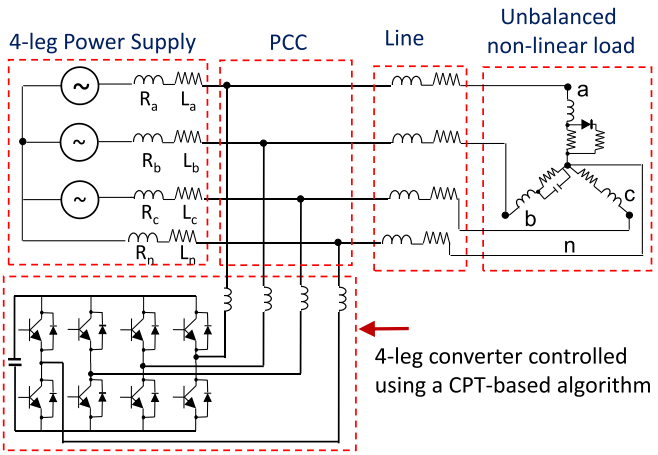

Fig. 1. Proposed control strategy for a four-leg compensator connected to a distribution network.

the signals and the generation of unwanted current components in some operating conditions [19], [20].

The experimental validation of the control systems and hardware topologies proposed in this paper has been partly based on the operating conditions of a real MG implemented in the north of Canada. The values of total harmonic distortion (THD), current imbalance, and variations of the load are based on the experimental data measured at this location. From these data (see Table I and Section IV), it is concluded that the zero sequence current components can have a relatively large magnitude when a real case of an isolated MG operating at a remote location is considered. Most of the previous publications related to the use of APFs in distributed generation are focused on three-leg applications without discussing the problems associated with low-voltage distribution systems that are mainly four-wire systems. Therefore, in this paper, the control of a four-leg APF based on the conservative power theory (CPT) is presented. Unlike previous publication where a four-leg converter is controlled using a fixed duty cycle of 50% in the fourth leg (see [21]), in this paper, full utilization of the dc link is achieved using proper modulation algorithms and control systems. In addition, resonant controllers instead of low dynamic controllers, as those reported in [21] and [22], are designed and implemented in this application.

Using a CPT-based algorithm is relatively simple to separate the unwanted current into several decoupled components, for instance, calculating which components are produced by unbalanced or nonlinear loads and which are due to power supply distortion (for accountability purposes [23], [24]). This is important considering that a typical MG has several power converters interfacing the intermittent NCRE sources to the MG. Therefore, it would be advantageous to use the residual VA capability of these converters to share the compensation of unwanted currents. This in turn could reduce the rating of the APF.

The proposed compensating topology is shown in Fig. 1. On the left-hand side, the Thévenin equivalent combination of the four-leg power supplies, obtained at the point of common coupling (PCC), is shown. The linear/nonlinear load and the compensator are connected at the PCC. If an energy storage system is required, this could be connected to the dc link of the APF to provide active power to the MG. The contributions of this paper are as follows.

1) In MGs, relatively large variations in the electrical frequency may occur. The sensitivity to grid frequency variations is a known limitation of the CPT [21], [24], and this paper proposes and validates an implementation approach that shows limited impact of frequency variation on the APF performance. This is confirmed by the experimental results presented in this paper where the performance of the CPT-based power compensator algorithm has been experimentally evaluated during transient operation and under grid frequency variations. Unlike [21], [23]–[25], in this paper, the CPT is applied to four-wire systems considering full control of the four legs in the APF, to regulate the positive, negative, and zero sequence voltages synthesized by the power converter. This includes operation of the CPT compensator with single-phase nonlinear loads.
2) The current control is realized using seven paralleled-connected self-tuning resonant controllers in each phase. The tracking of the resonant frequency is realized using a tuning algorithm, based on the real-time discretization of controllers implemented using the bilinear transform with frequency prewarping. As discussed in [26], this discretization method has important advantages, in terms of preserving the resonant frequency accuracy, particularly when high-order harmonics have to be compensated for. To the best of the authors' knowledge, self-tuning adaptive algorithms for the bilinear transform with frequency prewarping have not been discussed in the literature where most of the reported applications are based on the conventional bilinear transform [27].

TABLE I
MG OPERATING CONDITIONS

Description	Values	Units
Active power abc	458.41	kW
Reactive power abc	78.69	kVAr
Voltage a RMS	605.09	V
Current a RMS	172.50	A
Current b RMS	333.07	A
Current c RMS	247.14	A
Current imbalance neg seq	18.70	A
Current imbalance zero seq	20.74	A
Current a THD	7.49	%
Current b THD	5.63	%
Current c THD	5.25	%

The rest of this paper is organized as follows. In Section II, the CPT is briefly introduced. In Section III, the proposed control systems for the four-leg APF are discussed. The operating conditions for the small MG in northern Canada are briefly described in Section IV. In Section V, the experimental results obtained from a small prototype are presented. Finally, an appraisal of the proposed methodology is summarized in Section VI.

II. CONSERVATIVE POWER THEORY

The CPT has been proposed as a new power theory to analyze distribution systems and MGs, where single-phase loads, nonlinear loads, and strong harmonic distortion could

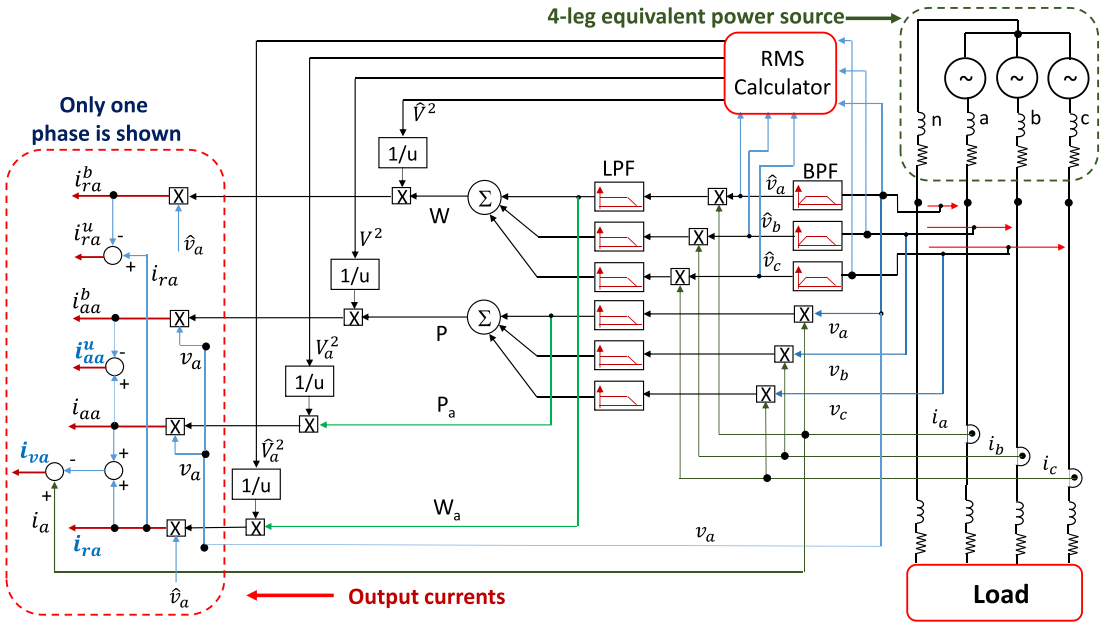

Fig. 2. Calculation of the compensating currents using the CPT. Only currents of phase A are shown.

be present [24], [25]. Using the CPT, an orthogonal separation of the unwanted current components can be achieved to allow selective compensation of them. Moreover, the implementation of a CPT-based control algorithm can be realized in the stationary *a–b–c* frame: it does not require a synchronous rotating reference frame [24]. The CPT has been discussed before (see [24], [28], [29]). However, for completeness, a brief introduction is presented here.

To implement the CPT, two instantaneous quantities are defined [24], [28]. The first is the instantaneous power that corresponds to the scalar product

$$p(t) = \boldsymbol{v} \circ \boldsymbol{i} = [v_a \quad v_b \quad v_c] \circ [i_a \quad i_b \quad i_c]^T. \tag{1}$$

The second is the instantaneous reactive energy defined as

$$w(t) = \hat{\boldsymbol{v}} \circ \boldsymbol{i} = [\hat{v}_a \quad \hat{v}_b \quad \hat{v}_c] \circ [i_a \quad i_b \quad i_c]^T \tag{2}$$

where $\hat{\boldsymbol{v}}$ is the vector containing the unbiased integral of the phase voltages. This vector $\hat{v}$ is calculated as

$$\hat{v}_\mu = \int_0^t v_\mu(\tau) d\tau - \bar{v}_{\int \mu}. \tag{3}$$

Note that the index "μ" ($\mu = a, b, c$) represents the variable per phase and the term $\bar{v}_{\int \mu}$, corresponds to the average component of each phase voltage integral. For the application depicted in Fig. 1, phase voltages are measured with respect to the neutral conductor at the PCC [24]. Considering the mean values of (1) and (2), the active power (P) and reactive energy (W) are defined as

$$P = \frac{1}{T}\int_0^T \boldsymbol{v} \circ \boldsymbol{i}\, dt \quad and W = \frac{1}{T}\int_0^T \hat{\boldsymbol{v}} \circ \boldsymbol{i}\, dt. \tag{4}$$

Based on (1)–(4), the load current can be decomposed in five orthogonal components. These are: 1) balanced active currents ($i^b_{a\mu}$); 2) balanced reactive currents ($i^b_{r\mu}$); 3) unbalanced active currents ($i^u_{a\mu}$); 4) unbalanced reactive currents ($i^u_{r\mu}$); and 5) void currents ($i_{v\mu}$) [24], [28].

The balanced active currents are defined as

$$i^b_{a\mu} = \frac{P}{V^2} v_\mu = G^b v_\mu \tag{5}$$

such that $\boldsymbol{V} = (V_a^2 + V_b^2 + V_c^2)^{1/2}$ is the collective RMS value (Euclidean norm) of the voltage, parameter G^b is the equivalent balanced conductance, and P is the active power.

The balanced reactive currents are defined as

$$i^b_{r\mu} = \frac{W}{\hat{V}^2} \hat{v}_\mu = \mathcal{B}^b \hat{v}_\mu \tag{6}$$

such that $\hat{v}_\mu$ is the unbiased voltage integral, $\hat{V}$ is the collective RMS value of the unbiased voltage integral, $\mathcal{B}^b$ is the equivalent balanced reactivity, and W is the reactive energy (see [24], [28]).

The *unbalanced currents* are defined as

$$i^u_\mu = i^u_{a\mu} + i^u_{r\mu} = (G_\mu - G^b) v_\mu + (\mathcal{B}_\mu - \mathcal{B}^b) \hat{v}_\mu \tag{7}$$

where the per-phase conductance and per-phase reactivity are defined as

$$G_\mu = \frac{P_\mu}{V_\mu^2} v_\mu \text{ and } \mathcal{B}_\mu = \frac{W_\mu}{\hat{V}_\mu^2} \hat{v}_\mu. \tag{8}$$

Note that the unbalanced currents (7) exist only if $G_\mu \neq G^b$ and/or if $\mathcal{B}_\mu \neq \mathcal{B}^b$, i.e., when the load is unbalanced. In single-phase circuit, the currents of (7) disappear.

The *void currents* are the remaining currents that do not transfer active or reactive energy, and are given by

$$i_{v\mu} = i_\mu - i^b_{a\mu} - i^b_{r\mu} - i^u_\mu. \tag{9}$$

All the current components (i.e., $i^b_{a\mu}, i^b_{r\mu}, i^u_{a\mu}, i^u_{r\mu}$, and $i_{v\mu}$) are orthogonal. The implementation of the CPT used in this paper is shown in Fig. 2. Voltage and current transducers are used to measure the load currents and voltages at the PCC. In this paper, a bandpass filter (BPF) is used to obtain the unbiased integral of the voltages (i.e., to obtain $[\hat{v}_a \ \hat{v}_b \ \hat{v}_c]$).

Note that this technique is widely used for the estimation of the magnetic flux in electrical machines [30]. The BPF eliminates the dc component of the signals and behaves as an ideal integrator for frequencies above ≈3 Hz (see [30]).

Low-pass filters (LPFs) are used to obtain the average value of the power P and the reactive energy W in each phase. The effective voltages and the Euclidian norms required by the CPT algorithm are calculated in the block labeled "RMS Calculator" shown at the top right of Fig. 2. This RMS calculator utilizes a filter with a transfer function equal to that used in the others LPFs shown in Fig. 2. This filter has been designed with a relatively high cut-off frequency to avoid jeopardizing the overall dynamic response. Note that the application of filters is also necessary to implement APFs based on other power theories, for instance, p–q power theory [19], [31].

As shown in the left-hand side of Fig. 2, the outputs of the CPT algorithm are the currents $[i^b_{a\mu}, i^u_{a\mu}, i^b_{r\mu}, i^u_{r\mu}, i_{v\mu}]$. These currents are used to calculate the references required by the current control.

An important remark related with the practical implementation of the CPT algorithm is the impact of grid frequency variations. As discussed above, the calculation of the unbiased integral (3), of the active power and reactive energy (4), and of the Euclidean norms requires BPFs or LPFs. In [21], these filters have been implemented using moving average digital filters, resulting in selective frequency responses but highly sensitive to grid frequency variations. From a practical perspective, moving average filters must be made frequency adaptive using the frequency measured by a phase-locked loop (PLL). This leads to considerable computational burden that might reduce the attractiveness of CPT-based filters. In this paper, a different approach has been considered: rather than implementing highly selective and adaptive filters, fixed filters with lower selectivity have been adopted. Considering that the range of frequency variations is expected to be narrow, the impact on filtering will also be limited. This choice simplifies the structure of the CPT algorithm, with limited impact on the effectiveness of the algorithm, as demonstrated in the experimental results under grid frequency transients.

A final comment about the implementation of the CPT is related with the practical need for complete current decomposition. If the APF is designed to fully compensate for the load nonidealities, only the balanced active components (5) of the load current must be evaluated, and all the remaining unwanted components can be derived subtracting the active balanced current from the load current. In this case, the computational burden of the CPT algorithm will be much reduced. On the other hand, if the APF has small power rating, or the active filtering is performed using the residual power capability of distributed generators, it might not be possible to compensate for the nonidealities in full, but an external command could be sent to another APF or power converter (with residual VA capability available) to demand for the compensation of a specific set of unwanted components. For the sake of generality, this paper addresses the case where a full current decomposition is implemented, giving maximum flexibility in the selection of the compensation objectives.

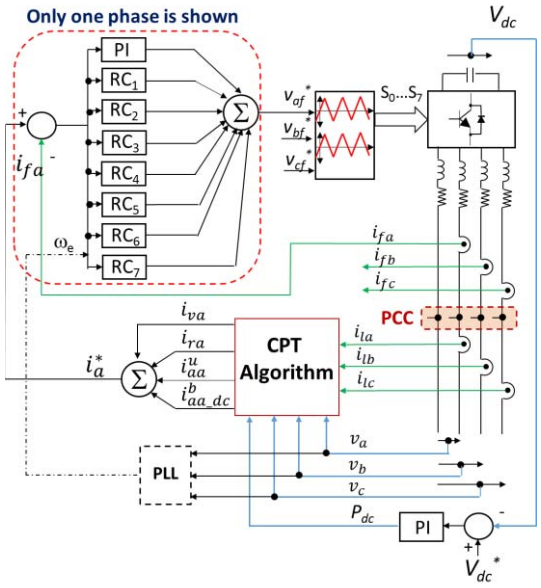

Fig. 3. Proposed current control system.

The capability of separating the unwanted signals into several orthogonal components (which can be compensated for using several power converters) is a very powerful feature of the CPT algorithm described in (1)–(9).

III. Proposed Control System

The proposed control system, for one of the phases, is shown in Fig. 3. In each phase, a PI controller and seven resonant controllers have been implemented in a parallel topology. The PI controller is required to compensate for the load dc components produced when nonlinear loads such as diode rectifiers are connected to the MG. The control system has been implemented in a–b–c coordinates.

Resonant controllers have been selected for this application because they can regulate sinusoidal signals with zero steady-state error in a–b–c coordinates. Moreover, they have better dynamic response than that obtained with other control topologies (e.g., repetitive controllers [22]). In each phase, a PI controller and seven resonant controllers, tuned to regulate the fundamental and the second-, third-, fourth-, fifth-, sixth-, and seventh-order harmonics, have been implemented in this paper. These frequencies have been selected considering the harmonic distortion presented in the case-study MG discussed in Section IV. However, in other cases, the elimination of more (or fewer) harmonic frequencies could be desirable by parallel connection of more resonant controllers.

Regarding implementation issues, it is well known that digital signal processors (DSPs) have experienced an exponential development in processing power [32]. Therefore, even if the proposed control algorithm, based on 21 self-tuning resonant controllers, seems relatively complex, it is simple to implement using a commercial DSP with a good processing capability and a suitable field-programmable gate array (FPGA) platform. For instance, the authors have implemented high-order resonant control systems using the low-cost Texas Instrument processor, TMS320C6713 DSK augmented with an Altera FPGA board

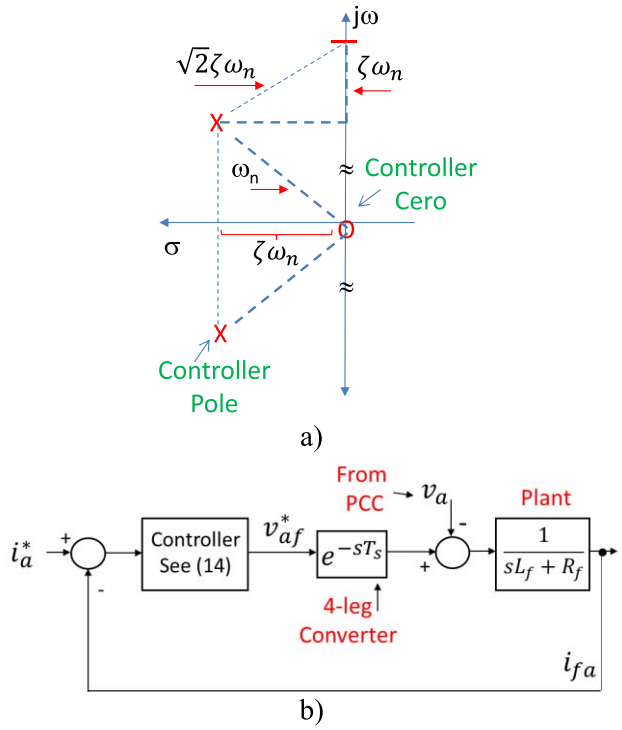

Fig. 4. (a) Pole and zero placement of the resonant part of the PR controller [see the right-side term of (10)]. (b) Control system considering the plant and the converter.

(see [33]). A detailed analysis of implementation issues is considered outside the scope of this paper.

In a parallel topology, each resonant controller can be separately designed assuming that the response of each controller is selective and alters only the frequency response around its resonant peak [34]. This simplifies the design procedure significantly.

A. Control System Design

The design and digital implementation of proportional resonant (PRs) controllers has been broadly discussed in previous publications (see [26], [33]–[35]) and is briefly summarized here.

In the s-plane, a PR controller, designed to regulate a current of frequency ω_j, can be written as

$$G_{cj}(s) = k_{pj} + \frac{k_{ij}s}{s^2 + 2\zeta\omega_j s + \omega_j^2} \tag{10}$$

where ζ is the controller damping and k_{pj} and k_{ij} are the controller gains. Note that (10) is equivalent to the transfer function of a PI controller when $\omega_j = 0$.

The poles and zero of the resonant part of the PR controller [see the right-side term of (10)] are shown in Fig. 4(a). Note that in this graph, ω_j is defined as $\omega_j = \omega_n$. Using Fig. 4(a) and the pole–zero placement method is relatively simple to design the term $\omega_c = \zeta\omega_j$ in order to achieve a given bandwidth [36].

Assuming that the term ω_c in (10) is very small compared with ω_n, the peak amplitude (P) of the resonant part of the controller is obtained when $s = j\omega_n$. From Fig. 4(a), it is also simple to conclude that for $s = j(\omega_n + \omega_c)$ and $s = j(\omega_n - \omega_c)$,

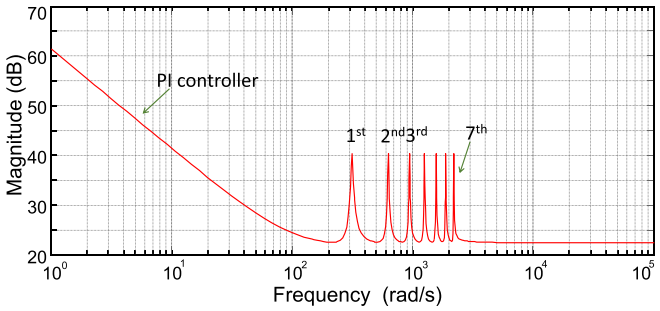

Fig. 5. Bode diagram of the current control system.

the gain is reduced in ≈3 dB, corresponding to an amplitude value of $P/\sqrt{2}$. Therefore, the term ω_c could be used to set the bandpass of the resonant frequency and helps to modify the selectivity of the PR controller of (10) (see [36]). In this paper, $\omega_c = 5$ rads^{-1} has been selected and this value allows to achieve good dynamic performance in the current control loop, as demonstrated by the experimental results presented in this paper.

The control diagram for design purposes is shown in Fig. 4(b). Assuming that each controller could be separately designed and that the voltage at the PCC is an external perturbation (unaffected by the operation of the APF), the following transfer function can be derived from Fig. 4(b):

$$\frac{i_{fa}}{i_a^*} = \frac{G_{cj}(s)\text{Plant}(s)e^{-ST_s}}{1 + G_{cj}(s)\text{Plant}(s)e^{-ST_s}} \tag{11}$$

where the term plant is defined as plant$(s) = 1/(sL_f + R_f)$ and i_{fa} is the current injected by the active filter in the phase "a" (see Fig. 3). Note that L_f and R_f are the inductance and the resistance per phase (respectively) of the impedance connecting the APF to the PCC. A delay of one sample in (11) is used to represent the transfer function of the four-leg APF. This delay is a simplified representation of the effects associated with the power converter modulation algorithm.

Adding the transfer functions of the controllers depicted in Fig. 3, the transfer function of the whole current control system (phase A) is obtained as

$$\frac{v_{af}^*(s)}{\left[i_a^*(s) - i_{fa}(s)\right]} = k_{pT} + \sum_{j=0}^{7}\left[\frac{k_{ij}s}{s^2 + 2\zeta\omega_j s + \omega_j^2}\right] \tag{12}$$

where $k_{pT} = \sum k_{pj}$ is the overall controller gain. Note that (12) includes the PI controller.

There are many control design methods reported in the literature for determining the controller gains k_{pj} and k_{ij} [see (10)] [33], [34]. In this paper, linear control tools such as Bode diagrams and root locus reshaping have been applied to design each of the eight parallel controllers shown in Fig. 3. Assuming that the resonant controllers alter only the frequency response around their own resonant frequency, each controller (as shown in Fig. 3) has been designed for a phase margin of at least 50° and a bandwidth of ≈30 rads^{-1}. The Bode diagram of the proposed control system is shown in Fig. 5.

In this paper, the z-plane implementation of (10) is realized by applying the bilinear transform with frequency prewarping

to (12). This discretization method has been selected because it preserves, with relatively good accuracy, the resonant frequency and the phase margin of the original design in the "s"-plane [26], [34]. Therefore, the digital version of (12) is obtained by replacing the Laplace operator "s" using

$$s = \frac{\omega_j}{\tan\left(\omega_j \frac{T_s}{2}\right)}\left(\frac{z-1}{z+1}\right) = k_{T\omega_j}\left(\frac{z-1}{z+1}\right) \tag{13}$$

where ω_j is the jth controller resonant frequency, T_s is the sampling period, and $k_{T\omega_j}$ is a nonlinear function of the resonant and sampling frequencies. Replacing (13) in (12), the z-plane transfer function of the current control system is obtained as

Note that (14), as shown at the bottom of this page, is the transfer function of a self-tuning resonant control system, which can be used to maintain the control system tuned in spite of changes in the fundamental frequency ($\omega_e = \omega_1$). In this paper, the value of ω_1 is estimated using a PLL (as shown in Fig. 3) and used to recalculate the values of $k_{T\omega_j}$ in (13) and (14), updating the controller coefficients.

To the best of our knowledge, the implementation of self-tuning resonant controllers, using the bilinear transform with frequency prewarping, has not been reported before.

B. Current Components Supplied by the APF

As shown in Fig. 2 and from (5)–(9), the CPT algorithm separates the load current into five orthogonal components $[i^b_{a\mu}, i^u_{a\mu}, i^b_{r\mu}, i^u_{r\mu}, i_{\upsilon\mu}]$. It is assumed that the load active balanced current $i^b_{a\mu}$ is supplied by the power source, and all the other components are supplied by the APF. Therefore, the unwanted current components being compensated for by the APF are obtained as

$$i^*_\mu = i^u_{a\mu} + i_{r\mu} + i_{\upsilon\mu} \tag{15}$$

where $i_{r\mu} = i^b_{r\mu} + i^u_{r\mu}$ [see (6) and (7)]. If the dc-link capacitor of Fig. 1 is floating, the four-leg APF has to supply the converter losses from the grid. Therefore, a balanced active current component has to be added to (15). This is obtained as

$$i^b_{a\mu\_\mathrm{dc}} = \frac{P_{\mathrm{dc}}}{\boldsymbol{V}^2}\upsilon_\mu \tag{16}$$

where P_{dc} is obtained from a PI controller (as shown in Fig. 3). Using (15) and (16), the current references are obtained as

$$i^*_\mu = i^u_{a\mu} + i_{r\mu} + i_{\upsilon\mu} + i^b_{a\mu\_\mathrm{dc}}. \tag{17}$$

As shown in Fig. 3, the current references (i^*_a, i^*_b, and i^*_c) are processed by 24 controllers (eight per phase, see Fig. 3) generating three instantaneous voltages $\upsilon^*_{af}, \upsilon^*_{bf}$, and υ^*_{cf}. These voltages are modulated by the four-leg converter using a sine-weighted pulsewidth modulation algorithm implemented in the DSPACE experimental platform discussed in Section V. In order to achieve full utilization of the dc link, a common voltage component is added to the modulation signals of all the four legs, including the neutral leg. This additional component is derived according to the well-known min–max algorithm using the methodology proposed in [37] and [38]. This algorithm is briefly summarized in the following.

The phase to neutral voltages υ^*_{af}, υ^*_{bf}, and υ^*_{cf} are calculated as

$$\upsilon^*_{af} = \upsilon^*_{az} - \upsilon^*_{fz} \tag{18}$$

$$\upsilon^*_{bf} = \upsilon^*_{bz} - \upsilon^*_{fz} \tag{19}$$

$$\upsilon^*_{cf} = \upsilon^*_{cz} - \upsilon^*_{fz} \tag{20}$$

where the subscripts a, b, c, and f represent the four legs of the APF and the subscript "z" is used to identify a fictitious neutral point that is located at a midpoint in the dc-link capacitors. The additional component υ^*_{fz} of (18)–(20) is derived using the min–max algorithm [37], where the common component added to each modulation signal is

$$\upsilon^*_{fz} = -\frac{\min\left(\upsilon^*_{af}, \upsilon^*_{bf}, \upsilon^*_{cf}\right) + \max\left(\upsilon^*_{af}, \upsilon^*_{bf}, \upsilon^*_{cf}\right)}{2}. \tag{21}$$

This guarantees maximum line to neutral voltage generation capability and, therefore, maximum utilization of the dc-link voltage, which is favorably compared with simpler solutions where the fourth leg is modulated at 50% duty cycle and the peak line to neutral voltage is constrained to half the dc-link voltage [21]. It can also be shown that the min–max method discussed in [37] and [38] is equivalent to space vector modulation, and as a result, the line to neutral voltage could increase up to 15.4% when compared with the case where a 50% duty cycle is used for the fourth leg.

IV. Operating Condition of the Case-Study Microgrid

To validate the performance of the proposed compensator, the operating conditions of an MG located in the north of Canada have been analyzed. The population of this community is about 1000 inhabitants.

The MG power sources are three diesel generators (0.4, 0.6, and 1 MW), 3 × 10 kW Bergey wind turbines, a 30-kW Wenvor wind turbine, and a 10-kW solar PV array. Fig. 6 shows the unifiliar diagram of the MG power system. The operating conditions, measured during the summer season, are presented in Table I. For the experimental work, the unbalanced currents shown in Table I were scaled, using per unit analysis, to currents that could be handled by the experimental prototype built at the Power Electronic Lab, University of Chile.

It is important to highlight that the values shown in Table I were used to set the minimum operating conditions for the

$$\frac{\upsilon^*_{af}(z)}{\left[i^*_a(z) - i_{fa}(z)\right]} = k_{pT} + \sum_0^7 \left[\frac{k_{T\omega_j} k_{ij}(z^2-1)}{\left(2\zeta\omega_j k_{T\omega_j} + k^2_{T\omega_j} + \omega^2_j\right)z^2 + 2\left(\omega^2_j - k^2_{T\omega_j}\right)z + \left(k^2_{T\omega_j} + \omega^2_j - 2\zeta\omega_j k_{T\omega_j}\right)}\right] \tag{14}$$

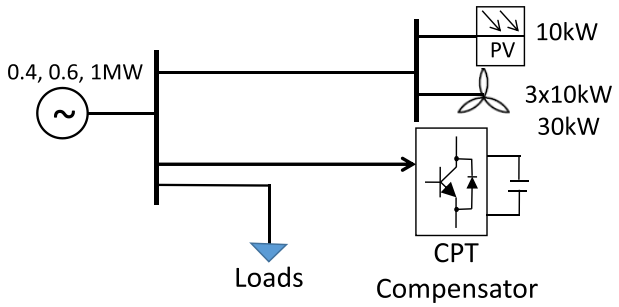

Fig. 6. Unifiliar diagram of the case-study MG.

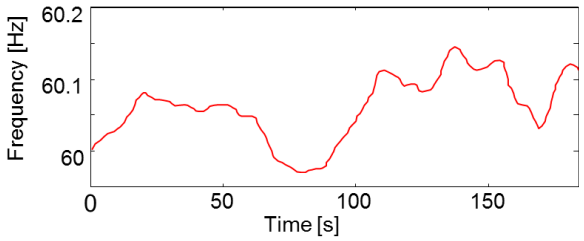

Fig. 7. Frequency variation.

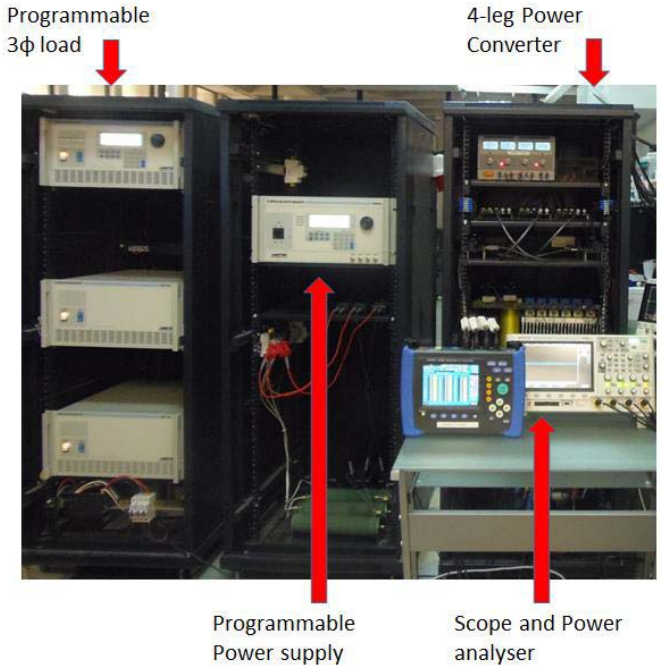

Fig. 8. Experimental system.

proposed APF. However, in order to test the performance of the proposed system considering the worst case situation, in some of the experimental results discussed in the next section, higher values of THDs, than those shown in Table I, were used.

The frequency variation of the MG used as the case study in this paper is shown in Fig. 7. However, for the experimental work presented in this paper, the base frequency is set to 50 Hz corresponding to the nominal frequency used in Chile.

V. Experimental Results

The control systems depicted in Fig. 3 have been implemented in the experimental system shown in Fig. 8. In this paper, an Ametek four-wire programmable power supply emulates the four-leg power supply shown in Fig. 1. An Ametek three-phase programmable load of 9 kW (left side of Fig. 8) is used to emulate linear/nonlinear load profiles replicating the operation conditions discussed in Section IV (Table I).

A four-leg voltage source power converter, based on the Semikron SKM50GB123D IGBT module, was designed and built for this paper. The control system shown in Fig. 2 is embedded in a DSPACE 1103 platform. The computational time of the proposed control system composed of resonant controllers, LPF/BPF, etc., is less than 50 μs. Hall effect transducers are used to measure the voltages and currents required for the implementation of the CPT algorithm shown in Fig. 3. A switching frequency of 5 kHz is utilized in the four-leg power compensator. To analyze the power quality, a Hioki 3196 power analyzer has been used in this paper.

Optical fiber links are used to transmit the switching signals S_o–S_7 (see Fig. 3) required to modulate the voltages v^*_{az}, v^*_{bz}, v^*_{cz}, and v^*_{fz} in the four-leg power converter.

A. Control System Performance for Unbalanced Operation

The performance of the CPT-based four-leg APF compensating a linear unbalanced system is shown in Fig. 9. An unbalanced four-wire resistive load of 10, 19.6, and 13.5 Ω has been programmed in the 3φ load. With these resistors, scaled values of the load currents shown in Table I (i.e., 333.07, 247.14, and 172.5 A) are produced. The power source is controlled to supply a balanced voltage of 120 V peak, 50 Hz. The dc-link voltage of the four-leg converter is regulated at 400 V.

Fig. 9(a) shows the power supply currents. Note that between 0 and 0.25 s, the compensator control system is disabled and the power supply current is heavily unbalanced with a peak current (phase A) of about 12 A. At $t = 0.25$ s, the control system is enabled and the APF supplies to the PCC the currents shown in Fig. 9(b), eliminating unwanted components from the power supply currents.

Fig. 9(c) shows an amplified view of Fig. 9(a). Note that the current waveforms have little distortion and the dynamic performance is good. The APF compensates for the power supply currents with a settling time of about 30–35 ms.

The dynamic performance of the CPT-based control algorithm has also been analyzed considering a load step in one of the phases. For this experimental test, the results were captured using a data acquisition interface. The experimental results are shown in Fig. 10. In this case, the APF control system is enabled for the whole test duration. Fig. 10(a) shows the step change in phase B, where the phase to neutral resistance is changed from 19.6 to 8 Ω ($t = 40$ ms) changing the phase B current from 10 to 15 A (peak). The magnitude of this load-step variation has been selected based on the values of the negative/zero sequence currents presented in Table I. Note that the peak currents in the other phases (A, C, and N) are not modified during this test.

Fig. 10(b) shows the power supply currents. After the load step, the APF compensates for the power supply currents in less than one cycle. For this test, fifth-order LPFs

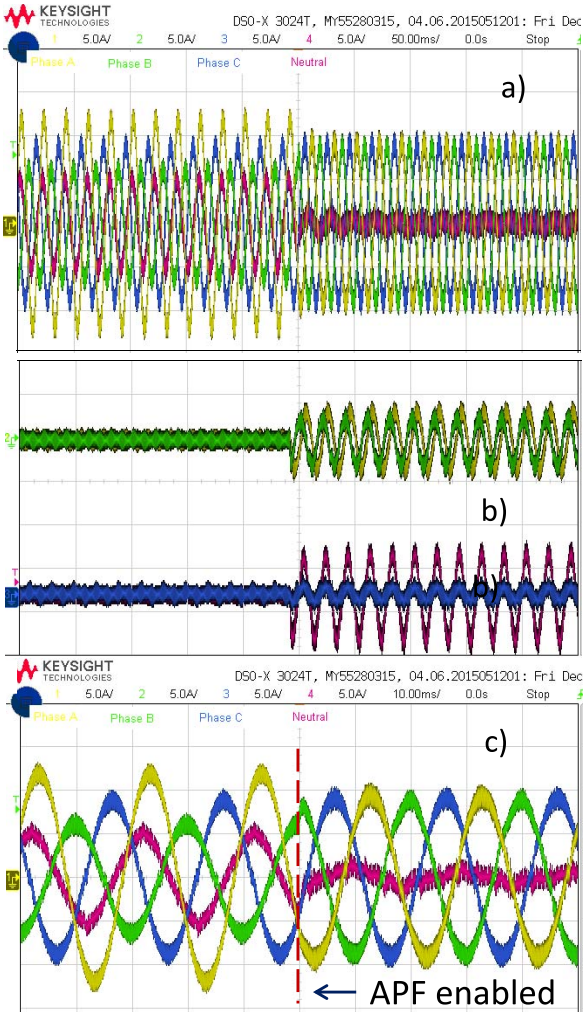

Fig. 9. Performance of the proposed APF compensating imbalances produced by a linear resistive load. (a) Currents in the power supply (5 A/50 ms/div). (b) Current supplied by the power compensator (5 A/50 ms/div). (c) Amplified view of (a) (5 A/10 ms/div).

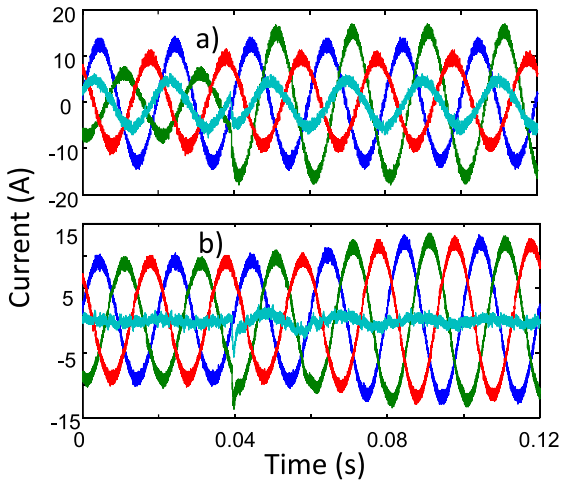

Fig. 10. Performance of the proposed control system for an unbalanced load step. (a) Load currents. (b) Power supply currents.

with a cut-off frequency of 20 Hz have been used in the implementation of the CPT algorithm shown in Fig. 2

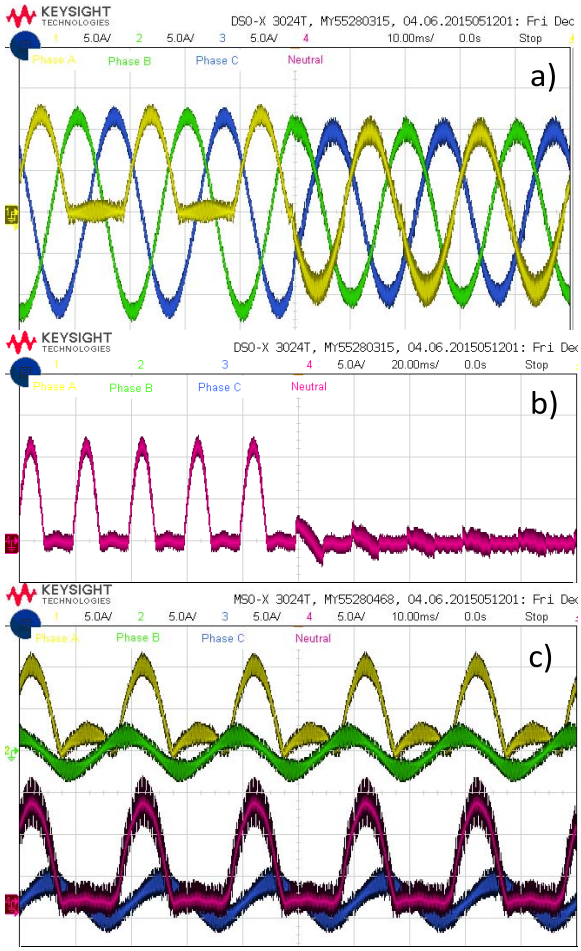

Fig. 11. Performance of the proposed control algorithm compensating nonlinear loads. (a) Power supply currents before and after enabling the APF (10 ms/5 A/div). (b) Neutral current corresponding to the test of Fig. 11(a) (20 ms/5 A/div). (c) Currents supplied by the APF to the PCC (10 ms/div-5 A/div).

(see the block labeled LPF). The BPF is also implemented using a fifth-order transfer function. As discussed in Section II, this BPF eliminates the dc component and behaves as an ideal integrator for frequencies above ≈3 Hz.

B. Control System Performance Considering a Nonlinear Load

To evaluate the performance of the proposed control system to reduce the harmonic distortion in the power supply currents, a nonlinear load was implemented using a star-connected four-wire load of 10 Ω per phase. A rectifier diode was serially connected to the resistor of phase A. In Fig. 11(a), the power supply currents are shown. Initially, the control system is disabled and only the positive semicycle of the phase A current is flowing. In $t = 50$ ms, the APF is enabled, and after a relatively fast transient, the current in the power supply becomes well balanced and undistorted. Fig. 11(b) depicts the neutral current, showing that before compensation, the power supply current has a strong zero sequence current component that is heavily distorted.

Fig. 11(c) shows the steady-state currents supplied by the APF. The currents in phase A and in the neutral wire have large peak values that are injected to the system in

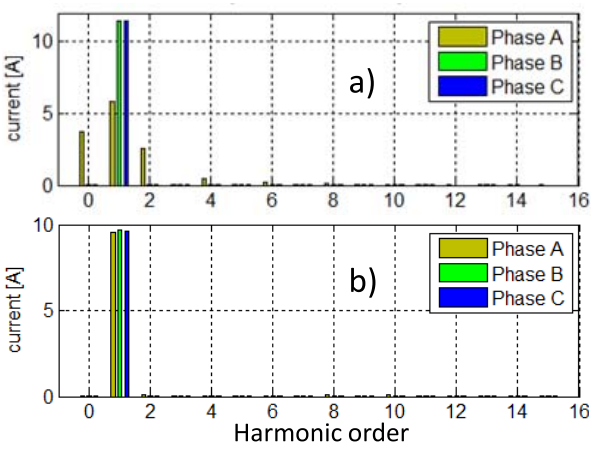

Fig. 12. Spectral estimation of the power supply currents. (a) Without compensation. (b) With the proposed four-leg APF.

order to eliminate unwanted components (imbalances and reactive and void currents) from the power supply. The THD is compensated for using the proposed methodology. Without the compensator [for $t < 50$ ms in Fig. 11(a)], the THDs for the power supply currents are 44.47%, 0.4%, and 0.4% (phases A, B, and C, respectively). After the control system is enabled, the THD in phase A is reduced to 2.27%. In the other two phases, the THD is little affected by the operation of the APF, maintaining similar values during the whole test. The spectrum of the power supply currents, corresponding to the experimental test depicted in Fig. 11, is shown in Fig. 12. Fig. 12(a) shows the magnitude of the harmonics before the APF control system is enabled. Note that in phase A, where a nonlinear load is connected, there is a strong dc component and even harmonics (mainly second and fourth) produced by the rectifier diode. When the CPT-based control system is enabled, the harmonics are almost eliminated and there is a significant reduction in the distortion of the power supply currents.

One of the reported advantages of the CPT [25], [28] is that the load current can be separated into current components that can be compensated for by different power converters located in the MG, e.g., using the residual VA capability of the power converters interfacing PV and wind energy in Fig. 6. Fig. 13(a) shows a distorted and unbalanced load current that has been obtained by modifying the crest factor, in each phase, of the Ametek programmable load. For this load, the current has been separated into the currents defined by (5)–(7). This separation has been realized by the DSPACE platform in real-time operation. Fig. 13(b) shows the balanced active currents [see (5)]. As mentioned before, this current is supplied by the four-leg power source (as shown in Fig. 1). Fig. 13(c) shows the unbalanced active current component [as shown in (7)], which is supplied by the APF. The unbalanced reactive current components are shown in Fig. 13(d); finally, the void current is shown in Fig. 13(e). For this experimental test, the balanced reactive currents have a negligible magnitude and they are not shown in Fig. 13. Finally, in Fig. 14, the compensated power supply currents, corresponding to the load currents of Fig. 13(a), are shown.

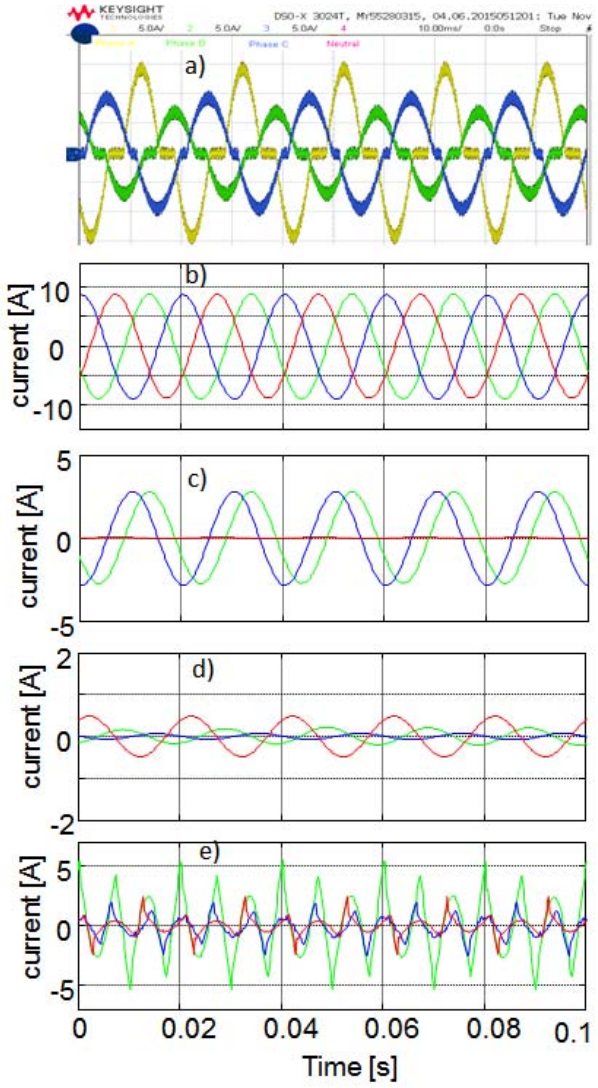

Fig. 13. Separation of the load current components using the CPT. (a) Load currents. (b) Balanced active current. (c) Unbalanced active currents. (d) Unbalanced reactive currents. (e) Void currents.

C. Operation of the Proposed Four-Leg APF Considering Frequency Variations

The electrical frequency of an MG can be subjected to relatively large variations, e.g., produced by the application of $P-f$ droop control or due to the effect of intermittent generation from renewable sources (see Fig. 7). For the correct operation of the proposed control system, self-tuning resonant controllers have been implemented in this paper.

In the experimental implementation discussed in this paper, tuning of the resonant controller is achieved by the online calculation of the $k_{T\omega_j}$ values [as shown in (13) and (14)] required by the bilinear transform with frequency prewarping. In addition, a PLL is necessary to estimate the fundamental frequency of the network (as shown in Fig. 3).

To test the performance of the self-tuning resonant control system, the programmable power supply used in this paper is controlled using the frequency profile depicted in Fig. 15. Note that this profile is a piecewise linearization of that shown in Fig. 7 with some modifications. For instance, the duration of

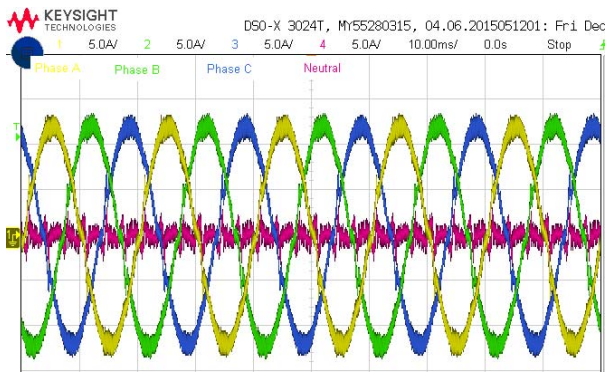

Fig. 14. Power supply currents corresponding to the experimental test of Fig. 13(a) (10 ms/div-5 A/div).

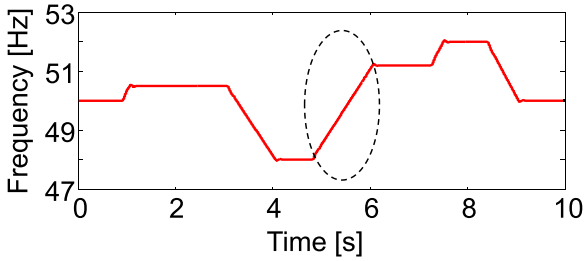

Fig. 15. Frequency profile used in this paper.

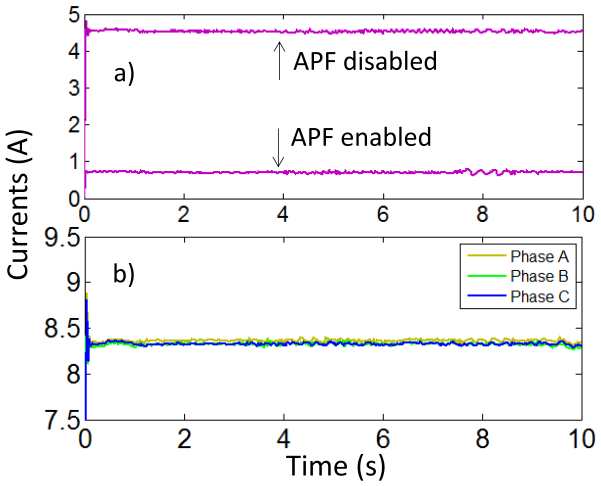

Fig. 16. Effective (RMS) currents circulating in the programmable power supply. (a) Power supply neutral current before and after enabling the APF. (b) Power supply phase currents considering the active filter enabled.

the profile has been reduced to 10 s and the frequency variation is larger (48–52 Hz). Moreover (as mentioned before), the nominal electrical frequency used in this paper is 50 Hz instead of the 60 Hz utilized for the frequency profile shown in Fig. 7.

The performance of the self-tuning algorithm has been tested considering operation of the system, feeding a load programmed with the current profile depicted in Fig. 13(a) and subjected, during 10 s, to the frequency variations shown in Fig. 15. Fig. 16 shows the currents in the programmable power supply (captured using the DSPACE data acquisition system). Note that effective currents are shown because of the problems associated with displaying the instantaneous currents for 10 s.

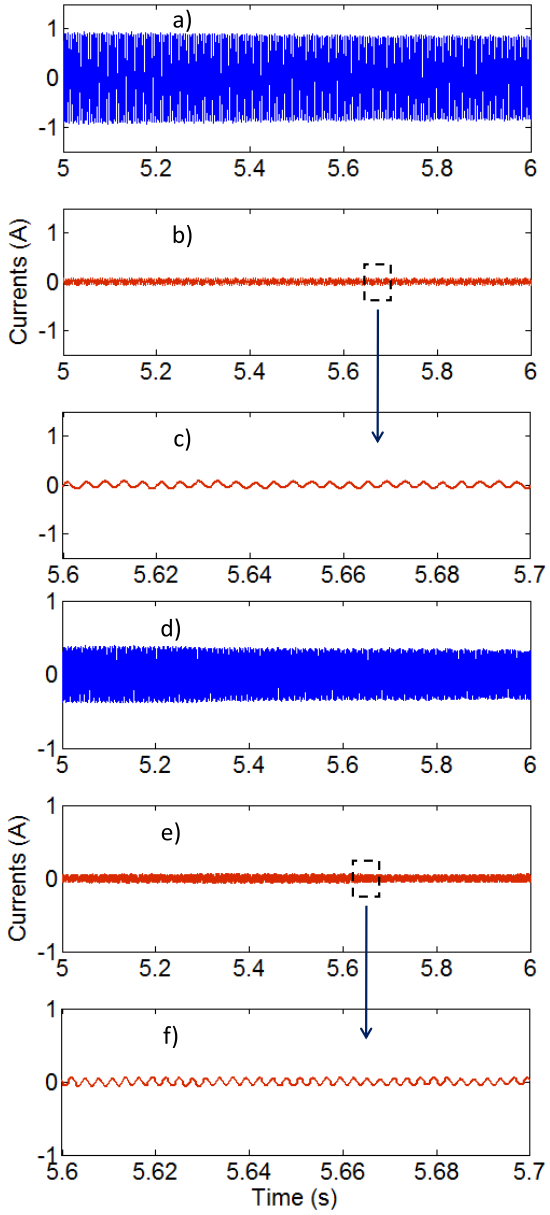

Fig. 17. (a) Fifth harmonic produced by the load current of Fig. 13(a). (b) Fifth harmonic component compensated in the power supply during a relatively fast frequency transient. (c) Amplified view of (b). (d) Seventh harmonic produced by the load current of Fig. 13(a). (e) Seventh harmonic component compensated in the power supply during the same frequency transient. (f) Amplified view of (e).

When the power compensator is enabled, the neutral current shown in Fig. 16(a) is reduced to a small value produced by the zero sequence harmonics that are not compensated for by the APF. As shown in Fig. 16(b), in the phases of the programmable power supply, the effective currents are well balanced. However, because effective currents by themselves cannot be used to demonstrate that the self-tuning algorithm is well tuned, an additional test is proposed and realized in this paper. Frequency-adaptive filters have been programmed to process the data captured by the DSPACE platform. The filters are designed to isolate the fifth and seventh harmonics of phase B in the load and power source currents.

In Fig. 17(a) and (b), the fifth harmonics of the load and power supply currents are depicted between $t = 5$ and 6 s

(see Fig. 15). Note that the frequency is varying between $f_e = 48$ and 51 Hz during that period of time. As shown in Fig. 17(a), the amplitude of the fifth harmonic in the load current is about 7.1% of the peak current. Fig. 17(b) shows the fifth harmonic component in the power supply current. Even with the relatively large frequency variation produced in this time period, the harmonic has been compensated and its amplitude is only 0.075 A, a reduction of 91% with respect to the uncompensated value. An amplified view of the fifth harmonic present in the power supply current is shown in Fig. 17(c).

Using the proposed methodology, the performance of the APF to reject the seventh harmonic has also been evaluated. Again the performance of the APF-based self-tuning resonant controllers is excellent, eliminating most of this harmonic from the power supply current as shown in Fig. 17(d)–(f). The amplitude of the seventh harmonic in the load current is about 3.33% of the peak current. However, the amplitude of the seventh harmonic in the power supply current is only 0.05 A, a reduction of 87.5% with respect to the uncompensated value.

VI. Conclusion

A new methodology for the control of a four-leg APF has been presented in this paper. The proposed control system is based on the CPT augmented with a PI and seven self-tuning resonant controllers in each phase. The compensation is achieved by regulating the positive, negative, and zero sequence voltages modulated by a four-leg voltage source converter.

The performance of the proposed control system has been tested considering the operating conditions of an MG located in northern Canada. Using per-unit analysis, the current and voltages have been referred to values that could be handled by the prototype implemented at the University of Chile. To evaluate the performance of the control system, balanced and unbalanced loads of linear/nonlinear nature, considering fixed/variable frequency operation have been applied at the PCC. In all the cases, the performance achieved by the proposed four-leg APF has been excellent.

The advantages of the CPT, as a new power theory for applications such as MGs where strong distortion and imbalances could be present, have also been demonstrated in this paper.

References

[1] C. Ahumada, R. Cárdenas, D. Sáez, and J. M. Guerrero, "Secondary control strategies for frequency restoration in islanded microgrids with consideration of communication delays," *IEEE Trans. Smart Grid*, vol. 7, no. 3, pp. 1430–1441, May 2016.

[2] K. Strunz, E. Abbasi, and D. N. Huu, "DC microgrid for wind and solar power integration," *IEEE J. Emerg. Sel. Topics Power Electron.*, vol. 2, no. 1, pp. 115–126, Mar. 2014.

[3] Y. Huang, X. Yuan, J. Hu, P. Zhou, and D. Wang, "DC-bus voltage control stability affected by AC-bus voltage control in VSCs connected to weak AC grids," *IEEE Trans. Emerg. Sel. Topics Power Electron.*, vol. 4, no. 2, pp. 445–458, Jun. 2016.

[4] R. H. Lasseter, "MicroGrids," in *Proc. IEEE Power Eng. Soc. Winter Meeting*, vol. 1. Jan. 2002, pp. 305–308.

[5] M. Hamzeh, S. Emamian, H. Karimi, and J. Mahseredjian, "Robust control of an islanded microgrid under unbalanced and nonlinear load conditions," *IEEE Trans. Emerg. Sel. Topics Power Electron.*, vol. 4, no. 2, pp. 512–520, Jun. 2016.

[6] Y. Li, D. M. Vilathgamuwa, and P. C. Loh, "Microgrid power quality enhancement using a three-phase four-wire grid-interfacing compensator," *IEEE Trans. Ind. Appl.*, vol. 41, no. 6, pp. 1707–1719, Nov. 2005.

[7] Y. Yang, K. Zhou, and F. Blaabjerg, "Current harmonics from single-phase grid-connected inverters—Examination and suppression," *IEEE Trans. Emerg. Sel. Topics Power Electron.*, vol. 4, no. 1, pp. 221–233, Mar. 2016.

[8] S. P. Oe, E. Christopher, M. Sumner, S. Pholboon, M. Johnson, and S. A. Norman, "Microgrid unbalance compensator—Mitigating the negative effects of unbalanced microgrid operation," in *Proc. 4th IEEE/PES Innov. Smart Grid Technol. Eur. (ISGT Europe)*, Copenhagen, Denmark, Oct. 2013, pp. 1–5.

[9] D. Sreenivasarao, P. Agarwal, and B. Das, "Neutral current compensation in three-phase, four-wire systems: A review," *Elect. Power Syst. Res.*, vol. 86, pp. 170–180, May 2012.

[10] E. Nasr-Azadani, C. A. Cañizares, D. E. Olivares, and K. Bhattacharya, "Stability analysis of unbalanced distribution systems with synchronous machine and DFIG based distributed generators," *IEEE Trans. Smart Grid*, vol. 5, no. 5, pp. 2326–2338, Sep. 2014.

[11] R. H. Salim, R. A. Ramos, and N. G. Bretas, "Analysis of the small signal dynamic performance of synchronous generators under unbalanced operating conditions," in *Proc. IEEE Power Energy Soc. General Meeting*, Minneapolis, MN, USA, Jul. 2010, pp. 1–6.

[12] J.-C. Wu, H.-L. Jou, K.-D. Wu, and H.-H. Hsiao, "Three-phase four-wire hybrid power filter using a smaller power converter," *Elect. Power Syst. Res.*, vol. 87, pp. 13–21, Jun. 2012.

[13] H. Yoshida and K. Wada, "Third-harmonic current suppression for power distribution systems under unbalanced installation of DG units," *IEEE Trans. Ind. Electron.*, vol. 62, no. 9, pp. 5578–5585, Sep. 2015.

[14] D. Kumar and F. Zare, "Harmonic analysis of grid connected power electronic systems in low voltage distribution networks," *IEEE Trans. Emerg. Sel. Topics Power Electron.*, vol. 4, no. 1, pp. 70–79, Mar. 2016.

[15] T.-L. Lee and P.-T. Cheng, "Design of a new cooperative harmonic filtering strategy for distributed generation interface converters in an islanding network," *IEEE Trans. Power Electron.*, vol. 22, no. 5, pp. 1919–1927, Sep. 2007.

[16] J. He, Y. W. Li, and M. S. Munir, "A flexible harmonic control approach through voltage-controlled DG–grid interfacing converters," *IEEE Trans. Ind. Electron.*, vol. 59, no. 1, pp. 444–455, Jan. 2012.

[17] M. Savaghebi, A. Jalilian, J. C. Vasquez, and J. M. Guerrero, "Autonomous voltage unbalance compensation in an islanded droop-controlled microgrid," *IEEE Trans. Ind. Electron.*, vol. 60, no. 4, pp. 1390–1402, Apr. 2013.

[18] G.-H. Kim, C. Hwang, J.-H. Jeon, J.-B. Ahn, and E.-S. Kim, "A novel three-phase four-leg inverter based load unbalance compensator for stand-alone microgrid," *Int. J. Elect. Power Energy Syst.*, no. 65, pp. 70–75, Feb. 2015.

[19] L. S. Czarnecki, "On some misinterpretations of the instantaneous reactive power p-q theory," *IEEE Trans. Power Electron.*, vol. 19, no. 3, pp. 828–836, May 2004.

[20] L. S. Czarnecki, "Effect of supply voltage harmonics on IRP-based switching compensator control," *IEEE Trans. Power Electron.*, vol. 24, no. 2, pp. 483–488, Feb. 2009.

[21] D. I. Brandao, H. K. M. Paredes, A. Costabeber, and F. P. Marafão, "Flexible active compensation based on load conformity factors applied to non-sinusoidal and asymmetrical voltage conditions," *IET Power Electron.*, vol. 9, no. 2, pp. 356–364, 2016.

[22] A. Lidozzi, C. Ji, L. Sodero, P. Zanchetta, and F. Crescimbini, "Resonant–repetitive combined control for stand-alone power supply units," *IEEE Trans. Ind. Appl.*, vol. 51, no. 6, pp. 4653–4663, Nov./Dec. 2015.

[23] P. Tenti, H. K. M. Paredes, F. P. Marafao, and P. Mattavelli, "Accountability in smart microgrids based on conservative power theory," *IEEE Trans. Instrum. Meas.*, vol. 60, no. 9, pp. 3058–3069, Sep. 2011.

[24] P. Tenti, H. K. M. Paredes, and P. Mattavelli, "Conservative power theory, a framework to approach control and accountability issues in smart microgrids," *IEEE Trans. Power Electron.*, vol. 26, no. 3, pp. 664–673, Mar. 2011.

[25] P. Tenti, A. Costabeber, P. Mattavelli, F. P. Marafao, and H. K. M. Paredes, "Load characterization and revenue metering under non-sinusoidal and asymmetrical operation," *IEEE Trans. Instrum. Meas.*, vol. 63, no. 2, pp. 422–431, Feb. 2014.

[26] A. G. Yepes, F. D. Freijedo, J. Doval-Gandoy, Ó. López, J. Malvar, and P. Fernandez-Comesaña, "Effects of discretization methods on the performance of resonant controllers," *IEEE Trans. Power Electron.*, vol. 25, no. 7, pp. 1692–1712, Jul. 2010.
[27] Z. Lin, S. Huang, and S. Wan, "A novel control scheme for T-type three-level SSG converters using adaptive PR controller with a variable frequency resonant PLL," *J. Power Electron.*, vol. 16, no. 3, pp. 1176–1189, May 2016.
[28] F. P. Marafão, D. I. Brandão, F. A. S. Gonçalves, and H. K. M. Paredes, "Decoupled reference generator for shunt active filters using the conservative power theory," *J. Control Autom. Elect. Syst.*, vol. 24, no. 4, pp. 522–534, 2013.
[29] T. S. Haugan and E. Tedeschi, "Active power filtering under non-ideal voltage conditions using the conservative power theory," in *Proc. IEEE 13th Brazilian Power Electron. Conf. 1st Southern Power Electron. Conf. (COBEP/SPEC)*, Fortaleza, Brazil, Nov. 2015, pp. 1–6.
[30] R. Pena, R. Cardenas, J. Proboste, G. Asher, and J. Clare, "Sensorless control of doubly-fed induction generators using a rotor-current-based MRAS observer," *IEEE Trans. Ind. Electron.*, vol. 55, no. 1, pp. 330–339, Jan. 2008.
[31] H. Akagi, E. H. Watanabe, and M. Aredes, *Instantaneous Power Theory and Applications to Power Conditioning*. Piscataway, NJ, USA: IEEE Press, 2007.
[32] S. Kouro, M. A. Perez, J. Rodriguez, A. M. Llor, and H. A. Young, "Model predictive control: MPC's role in the evolution of power electronics," *IEEE Ind. Electron. Mag.*, vol. 9, no. 4, pp. 8–21, Dec. 2015.
[33] R. Cardenas, C. Juri, R. Pena, J. Clare, and P. Wheeler, "Analysis and experimental validation of control systems for four-leg matrix converter applications," *IEEE Trans. Ind. Electron.*, vol. 59, no. 1, pp. 141–153, Jan. 2012.
[34] A. G. Yepes, F. D. Freijedo, Ó. López, and J. Doval-Gandoy, "Analysis and design of resonant current controllers for voltage-source converters by means of Nyquist diagrams and sensitivity function," *IEEE Trans. Ind. Electron.*, vol. 58, no. 11, pp. 5231–5250, Nov. 2011.
[35] A. Rodríguez, C. Girón, M. Rizo, V. Sáez, E. Bueno, and F. J. Rodríguez, "Comparison of current controllers based on repetitive-based control and second order generalized integrators for active power filters," in *Proc. 35th Annu. Conf. IEEE Ind. Electron. (IECON)*, Porto, Portugal, Nov. 2009, pp. 3223–3228.
[36] S. P. Oe, "Power quality improvement of microgrids, Nottingham," Ph.D. dissertation, Dept. Elect. Electron. Eng., Univ. Nottingham, Nottingham, U.K., 2014.
[37] J.-H. Kim and S.-K. Sul, "A carrier-based PWM method for three-phase four-leg voltage source converters," *IEEE Trans. Power Electron.*, vol. 19, no. 1, pp. 66–75, Jan. 2004.
[38] D. G. Holmes and Thomas A. Lipo, *Pulse Width Modulation for Power Converters: Principles and Practice*. Hoboken, NJ, USA: Wiley, 2003, p. 744.

Claudio Burgos-Mellado was born in Cunco, Chile. He received the B.Sc. and M.Sc. degrees in electrical engineering from the University of Chile, Santiago, Chile, in 2012 and 2013, respectively. He is currently pursuing the double-award Ph.D. program in electrical engineering with the University of Chile and the University of Nottingham, Nottingham, U.K.

His current research interests include battery energy storage systems, electrical vehicle technologies, power electronics, microgrids, and power quality.

Carlos Hernández-Carimán was born in Panguipulli, Chile. He received the B.Sc. degree in electronic engineering from the University of Concepción, Concepción, Chile, in 2013, and the M.Sc. degree in electrical engineering from the University of Chile, Santiago, Chile, in 2016.

His current research interests include four-leg active filter, power electronics, microgrids, and renewable energy systems.

Roberto Cárdenas (S'95–M'97–SM'07) was born in Punta Arenas, Chile. He received the B.S. degree from the University of Magallanes, Punta Arenas, in 1988, and the M.Sc. and Ph.D. degrees from the University of Nottingham, Nottingham, U.K., in 1992 and 1996, respectively.

He was a Lecturer with the University of Magallanes from 1989 to 1991 and from 1996 to 2008. From 1991 to 1996, he was with the Power Electronics Machines and Control Group, University of Nottingham. From 2009 to 2011, he was with the Electrical Engineering Department, University of Santiago, Santiago, Chile. He is currently a Full Professor of Power Electronics and Drives with the Electrical Engineering Department, University of Chile, Santiago, Chile. His current research interests include the control of electrical machines, variable speed drives, and renewable energy systems.

Doris Sáez (S'93–M'96–SM'05) was born in Panguipulli, Chile. She received the M.Sc. and Ph.D. degrees in electrical engineering from the Pontificia Universidad Católica de Chile, Santiago, Chile, in 1995 and 2000, respectively.

She is currently an Associate Professor with the Electrical Engineering Department, University of Chile, Santiago. She has authored or co-authored the books entitled *Hybrid Predictive Control for Dynamic Transport Problems* (Springer-Verlag, 2013) and *Optimization of Industrial Processes at Supervisory Level: Application to Control of Thermal Power Plants* (Springer-Verlag, 2002). Her current research interests include predictive control, fuzzy control design, fuzzy identification, control of power generation plants, and control of transport systems.

Dr. Sáez is an Associate Editor of the IEEE TRANSACTIONS ON FUZZY SYSTEMS.

Mark Sumner (SM'05) received the B.Eng. degree in electrical and electronic engineering from Leeds University, Leeds, U.K., in 1986, and the Ph.D. degree in induction motor drives from the University of Nottingham, Nottingham, U.K., in 1990.

He was with Rolls Royce Ltd, Ansty, U.K. In 1992, he joined as a Research Assistant and later became a Lecturer at the University of Nottingham, where he is currently a Professor of Electrical Energy Systems. His current research interests include the control of power electronic systems including sensorless motor drives, diagnostics and prognostics for drive systems, power electronics for enhanced power quality, and novel power system fault location strategies.

Alessandro Costabeber (S'09–M'13) received the B.S. Degree (Hons.) in electronic engineering and the Ph.D. degree in information engineering with a specialization on energy efficient architectures and control techniques for the development of future residential microgrids from the University of Padova, Padova, Italy, in 2008 and 2012, respectively.

From 2012 to 2014, he was a Research Fellow with the University of Padova. In 2014, he joined the Power Electronics Machines and Control Group, Department of Electrical and Electronic Engineering, University of Nottingham, Nottingham, U.K., as a Lecturer in Power Electronics. His current research interests include HVDC converters topologies, high-power density converters for aerospace applications, control solutions and stability analysis of ac and dc microgrids, control and modeling of power converters, power electronics, and control for distributed and renewable energy sources.

Dr. Costabeber was a recipient of the IEEE Joseph John Suozzi INTELEC Fellowship Award in Power Electronics in 2011.

Helmo K. Morales Paredes (S'10–M'11) received the B.S. degree in electrical engineering from the National University of Saint Agustine, Arequipa, Peru, in 2002, and the M.Sc. and Ph.D. degrees from the University of Campinas, Campinas, Brazil, in 2006 and 2011, respectively.

In 2009, he joined the Department of Information Engineering, University of Padova, Padova, Italy, as a Visiting Student. In 2014, he joined the PEMC Group, Department of Electrical and Electronic Engineering, University of Nottingham, Nottingham, U.K., as a Visiting Scholar. Since 2011, he has been an Assistant Professor with São Paulo State University (Unesp), Institute of Science and Technology, Sorocaba, Brazil, where he joined the Group of Automation and Integrating Systems. His current research interests include power quality, power theories and power electronics applied to local and/or cooperative control of compensators, accountability, revenue metering, and grid-connected converters for renewable energy systems and microgrids.

Dr. Morales Paredes is a member of the Brazilian Power Electronics Society, Brazilian Automatic Society, IEEE Power Electronics Society, and IEEE Industrial Electronics Society. He was a recipient of the Prize Paper Award in the IEEE TRANSACTIONS ON POWER ELECTRONICS in 2011.